LONG ENDURANCE ELECTRIC UAV FOR CIVILIAN SURVEILLANCE MISSIONS

André C. Marta*, Pedro V. Gamboa**
*LAETA, CCTAE, Instituto Superior Técnico, Universidade de Lisboa, Lisboa, Portugal
**Aerospace Sciences Department, Universidade da Beira Interior, Covilhã, Portugal
andre.marta@tecnico.ulisboa.pt; pgamboa@ubi.pt

Abstract

The design of a long endurance electric UAV is presented. The mission requirements are derived from civilian surveillance applications, such as forest, coast or border patrol. As such, long endurance is desired, which is tackled by a careful lightweight airframe design and an electric propulsion system assisted with solar cell arrays. The main steps of the design are covered, including numerical simulations, as well as construction, component and systems testing and flight testing. The feasibility of a green, low cost, small footprint UAV is demonstrated.

1 Introduction

Over the last decade, there has been a remarkable progress on Unmanned Aerial Vehicles (UAVs). Unfortunately, the main driver has been military applications, where the high risk missions make the absence of pilot highly desirable. However, there are a large number of civilian applications that can take advantage of this technological progress, such as fire detection and firefighting management, search and rescue missions, natural disaster areas survey, geographical or weather survey, wildlife surveillance, oil spill monitoring, environmental research and air quality monitoring, digital mapping and planning, among many others.

While the military fleet has been growing exponentially, the civilian side has not seen significant usage. To our view, this is due to four main reasons: the lack of regulations, the prohibitive cost, the operational complexity, and the typically large size of such aircrafts.

The first reason is presently being addressed. In the USA, the Federal Aviation Administration (FAA) [1] recently concluded the selection of six UAV test sites, which will surely boost the development of civilian systems. Also in its roadmap is the merging of UAV operations in the USA airspace system, likely to turn into reality in the next five years, which should help increasing the UAV usage by individuals or commercial companies. According to the report of the Association for Unmanned Vehicle Systems International [2], it is predicted that once approved, the UAS industry could create more than 100,000 jobs and generate $82 billion in economic impact in the first decade.

Surely commercial aspects dealing with legal, insurance and business operations requirements will be challenging but the last three reasons still prevent the creation of successful UAV businesses. Addressing cost, flexibility and portability, while guaranteeing considerable endurance/range is something it has to be considered from the very early stages of the design.

On 26 July 2013, the FAA certified the first UAV models to fly in U.S. airspace for commercial purposes: the AeroVironment RQ-20 Puma [3] and the Boeing Insitu Scan Eagle X200 [4]. The Puma is a small (2.8m span, 5.9kg MTOW), surveillance unmanned aircraft vehicle. It is hand-launched and battery powered, with a standard endurance of 2 hours and range of 15 km. Planed upgrades for the

near future include solar cells to increase endurance to 9 hours or enhanced batteries to increase endurance to 3.5 hours. The ScanEagle is also a small surveillance unmanned aerial vehicle (3.1m span, 22kg MTOW). It uses a pneumatic launcher and its 1.12 kW single-piston engine allows for long-endurance (over 20 hours). Both UAVs have been used by different armed forces and governments, thus benefited from previous military certification to swiftly achieve their commercial certification. These two highly sophisticated state-of-the-art systems comprise one or more vehicles, ground control station and launch and recovery systems, driving their cost to over three millions of dollars.

The use of solar cells has been tried in several aircrafts before. The last design was unveiled in April 2014, when the Solar Impulse team presented its Solar Impulse 2 plane [5]. This enhanced version was designed to fly around the world and it can theoretically remain in the air indefinitely. Interestingly, the team leaders, Piccard and Borschberg, have reportedly stated that the pilot is now the weakest link in the project, clearly acknowledging a UAV solution is the future.

Never the use of renewable energy has been more in demand by society, never the electric systems (solar panels, motors and batteries) have been so efficient nor the design tools (both numerical and experimental) have been so accessible to the designer. With this in mind, the main objective of this paper is to present the development of a low cost, small footprint long endurance electric UAV (LEEUAV), capable of being deployed from short airfields, easy to build and maintain, and highly flexible to perform different civilian surveillance missions. To accomplish the proposed goals, state-of-the-art analysis methods and out-of-the-shelf hardware are used, together with some innovations in terms of aircraft design and system integration solutions.

The material presented here is part of a collaborative research project involving three research units belonging to the research line of Aeronautics and Space of LAETA [6], namely CCTAE [7], AEROG [8] and IDMEC [9].

2 Aircraft Features

Among other features, the UAV specifications include:
• Long endurance: use of green power technologies (electric propulsion system with solar power), in particular using highly efficiency solar cells, high capacity/density batteries, efficient compact motors and appropriate long endurance aerodynamic design;
• Autonomous flight: vehicle equipped with auto-pilot navigation systems;
• High-strength, low-weight structure: use of composite materials, with fuselage/wing critical areas designed for good impact resistance on landing, using easy to manufacture techniques;
• Multiple mission: design for sufficiently large payload range capability and upgradeable modular avionics, to enable an easy software upload and/or hardware swap to meet the selected mission requirements.

3 Conceptual Design

The particular requirements of the UAV can only be fulfilled by thoughtful considerations and optimization so that a lightweight and aerodynamically efficient airframe is obtained resulting in a low power vehicle.

The mission for the LEEUAV was decided on a consortium meeting, having in mind the ultimate goal of having a vehicle capable of flying for long time with low power requirements carrying a payload of up to 1kg. The mission profile can be summarized as:
1. Takeoff in a very short distance (in 8 meters), or hand launched (in 3 meters);
2. Climb 1000 meters to cruise altitude in 10 minutes;
3. Fly for 8 hours in the equinox at low speed defined by system efficiency but greater than 7m/s;
4. Descent during 29 minutes without power;
5. Landing in the field.

Despite tailless UAV have shown superior aerodynamic and flight performance characteristics [10], a conventional wing and fuselage configuration was chosen to

29th Congress of the International Council
of the Aeronautical Sciences
St. Petersburg, Russia; September 7–12, 2014

accommodate the relatively bulky avionics. This configuration still provides high aerodynamic efficiency, allows a large wing without sweep to place the solar arrays and results in an inherently stable platform.

Several existing low Reynolds number (Re) airfoils were considered as candidates for the wings but due to the specific design requirements of this aircraft a new airfoil was developed using an in-house gradient-based aerodynamic shape optimization tool. The airfoil geometry obtained from design optimization exhibits low drag coefficient at low Re for its design lift coefficient range and it is shown in Fig. 1.
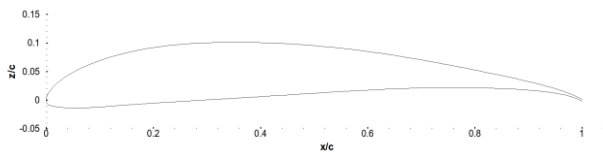

Fig. 1. LEEUAV airfoil geometry.

Obtaining the correct size of the aircraft is essential to produce a high performance design. The conceptual design was based on an extensive parametric study developed in-house in a spreadsheet whose primary design parameters were the wing span and the wing mean chord. Other parameters allowed to vary in the study were the cruise lift coefficient, the center of gravity (CG) position, the airfoil, the motor and the propeller. In the implemented tool, low fidelity models have been developed for various analysis of the vehicle: aerodynamics, stability and control, propulsion, weight and flight performance.

For a high aspect ratio wing (>6) the most important single factor to its aerodynamic performance is the airfoil. For that reason the aerodynamic model implemented uses interpolated values from 2D aerodynamic coefficients tables computed with XFOIL [11] for any given Reynolds number and angle of attack and then applies a 3D correction based on the wing aspect ratio. The weight model developed scales a given aircraft of similar layout and structure based on their individual components' weight and relative shape, size, ultimate load factor and maximum takeoff

weight (MTOW). Matching of the propeller and motor is performed for the propulsion model given a power setting or power required and a flight speed. This makes the absorbed power by the propeller equal to the shaft power enabling the calculation of thrust produced and electrical power consumed to be estimated in any flight situation. The horizontal and vertical tails are automatically sized for given longitudinal, lateral and directional static margins and low speed control requirements.
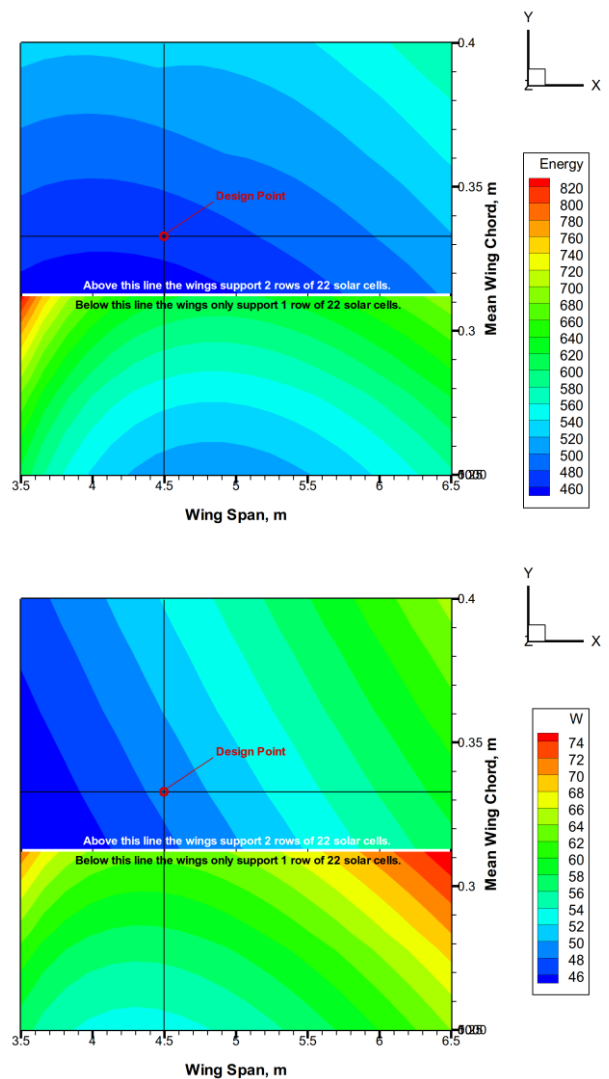

Fig. 2. Some results of the parametric study.

Since the motor power source was intended to provide 11.1V nominal voltage, multiples of 22 0.58V cells were considered in the analysis for the wing span interval selected between 3.5m and 6.5m. This individual voltage corresponds

to the maximum power point (V_{mpp}) for the selected solar cell (see Sec. 4.1). The energy model automatically sizes the batteries based on the solar cells available on the wing surface, on the mission duration, on the energy requirements for each mission segment and on the maximum electrical power required by the motor and systems.

Figure 2 shows some of the results of the parametric study for total flight energy used and takeoff weight. All solutions in this figure comply with the cruise endurance requirement, but not all are light and energy efficient. Below the horizontal white line represented in the figures the wing can only accommodate one row of solar cells whilst above that line two rows can be placed.

The design point was selected for a span of 4.5m and a mean wing chord of 0.33m as indicated in Fig. 2. These values allow for a large area which is important to flexibly apply the solar cells onto the wing upper surface and to provide the low speed cruise while approaching the solution which requires the least energy for the mission proposed. Adding to that, with the size selected the wing can also be built into three parts capable of being disassembled for transportation without significant complexity or penalty in wing mass. According to the parametric study, a slightly shorter span or smaller chord would produce a lighter and more energy efficient aircraft but, with the dimensions adopted, the payload can be somewhat increased in the future without significant negative effects on the overall performance of the vehicle. This capability is important because it rules out the need to redesign the wing. Table 1 shows a summary of the UAV main characteristics and Tab. 2 the UAV estimated main performance figures.

The top, front and side views of the UAV are shown in Fig. 3, reflecting the results of the parametric design as well as a structural concept definition, a weight and balance study and systems integration. Available area on the wing tip and horizontal stabilizer can be used in the future to place additional solar cells if deemed necessary to increase either the motor power or the systems power.

Span [m]	4.500
Length [m]	2.370
Root wing chord [m]	0.350
Tip wing chord [m]	0.250
Wing area [m^2]	1.518
Aspect ratio	13.500
Tailplane chord [m]	0.213
Tailplane span [m]	0.850
Tailplane area [m^2]	0.181
Root empennage chord [m]	0.258
Tip empennage chord [m]	0.364
Empennage area [m^2]	0.077
Structure mass [kg]	1.590
Empty mass [kg]	3.890
Takeoff mass [kg]	4.900

Tab. 1. Summary of UAV dimensions and weights.

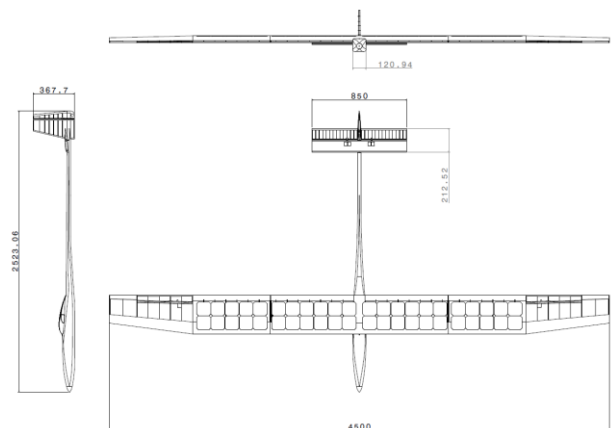| Cruise speed [m/s]	7.5
Maximum rate of climb [m/s]	2.2
Lift-to-drag ratio	20
Maximum speed [m/s]	21.1
Stall speed [m/s]	6.1
Takeoff roll distance [m]	8.1

Tab. 2. Summary of UAV estimated performance.

Fig. 3. CAD drawing views of UAV.

Fig. 4. CAD rendering of UAV.

The airframe concept was developed using a CAD system which enables to represent the

29th Congress of the International Council
of the Aeronautical Sciences
St. Petersburg, Russia; September 7–12, 2014

major structural components, to verify fittings and interfaces and to study the positioning of the systems for functionality, balance and ease of access. Figure 4 shows the complete airframe.

4 Preliminary Design

After completion of the conceptual design, each of the LEEUAV systems were subject to a careful in-depth design using not only high-fidelity analysis tools but also experimental testing.

4.1 Propulsion System

The use of solar energy in aviation offers advantages not only in terms of emissions and noise but also endurance, this latter particularly important in this project. Photovoltaic modules can be used to collect the energy of the sun during the day, one part being used directly to power the propulsion unit and on-board instruments, the other part being stored for the night time.

The conceptual design of the propulsion system resulted in an architecture completely different from the conventional methods of propulsion. It has determined a hybrid solution, using both lithium-polymer batteries and solar panels to provide energy to the electric motor.

The preliminary design of the propulsion system includes the development of a rigorous solar radiation model and a detailed analysis of the UAV mission and energy requirements. The proposed architecture of the propulsion system for the LEEUAV shown in Fig. 5 comprises six major components: the solar panels, the solar charge controller, the battery, the speed controller, the electric motor and the propeller.
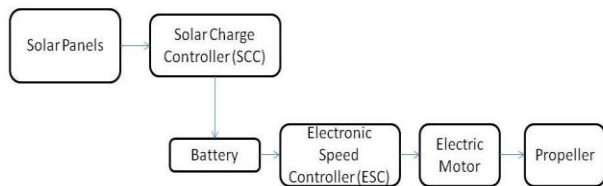

Fig. 5. Architecture of the propulsion system.

The airfoil design, shown in Fig. 1, also accounted for the suction side curvature since it is an important factor when attaching the solar panels that have limited flexibility.

The solar cells are to be installed on the wing upper surface. Because of limited flexibility of the solar panels to conform with the airfoil profile shape, an estimated area available S_{PV} was obtained using three correction factors applied to the wing reference area S_{ref}: curvature correction factor at the leading edge, CF_{LE} (15%), to correct the curvature excess in this area; correction factor at the trailing edge, CF_{TE} (10%), to account for the occupied area by the control surfaces; and the wingspan correction factor, CF_W (18%), to account for a safety zone at each wing tip. This led to an available area for installation of panels

$$c_{PV} = \frac{100 - CF_{LE} - CF_{TE}}{100} \cdot c, \qquad (1)$$

$$b_{PV} = \frac{100 - CF_W}{100} \cdot b, \qquad (2)$$

$$S_{PV} = c_{PV} \cdot b_{PV}, \qquad (3)$$

obtaining an available area S_{PV} of 0.728m^2.

The energy requirements have been calculated based on the efficiency of each component of the propulsion system in every stage of the mission. The efficiency of battery, cables and electronic speed controller ESC, is fixed for the entire mission while the efficiency of the electric motor and propeller are different in each stage. The power required for each stage of the mission can be estimated as

$$P_{req} = v_{stage} \cdot D_{stage}, \qquad (4)$$

where v_{stage} is the corresponding aircraft speed and D_{stage} is the aircraft drag. Knowing the duration of each stage t_{stage}, it is then possible to calculate the energy required at each stage of the mission,

$$E_{req} = P_{req} \cdot t_{stage}. \qquad (5)$$

The total efficiency of the components is estimated as

$$\eta_{stage} = \eta_B \cdot \eta_C \cdot \eta_{ESC} \cdot \eta_{M_{stage}} \cdot \eta_{P_{stage}}, \quad (6)$$

where η_B, η_C and η_{ESC} are the efficiency of battery, cables and electronic speed controller, common for all stages, and $\eta_{M_{stage}}$ and $\eta_{P_{stage}}$ are the efficiency of electric motor and propeller for the particular stage. Then the required energy can be determined as

$$E_{req} = \left(\frac{1}{\eta_{stage}} \cdot P_{req} \right) \cdot t_{stage} . \quad (7)$$

Table 3 summarizes the values of required electrical power and energy for each segment of the mission. It should be noted that the gravitational potential energy corresponding to 1000m altitude gain was added to the climb segment, and no power gliding was assumed in the descent.

Segment	η_T	P_{req} [W]	E_{req} [kJ]
Takeoff	15.9	451.2	0.4
Climb	22.4	444.7	266.9
Cruise	38.2	46.7	1370.9
Descent		0	0
TOTAL			1638.2

Tab. 3. Energy required for propulsion.

The total energy required (E_{req}=1638kJ) and the maximum electrical power required (P_{req}=451W) were used for the sizing of the propulsion system. Figure 6 shows the power distribution for the complete mission.
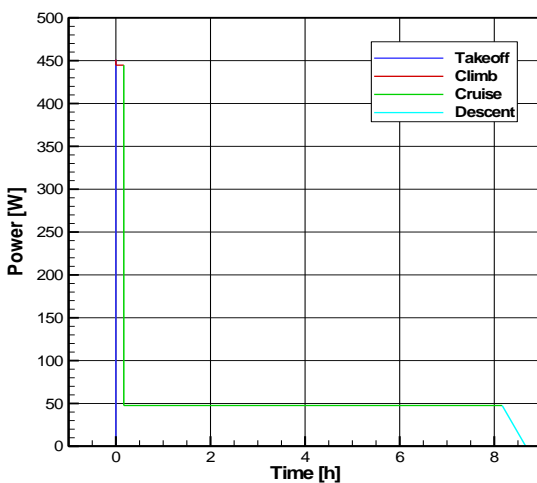

Fig. 6. Power required at every stage of the mission.

During the day, the propulsion energy of the electric UAV can be obtained by batteries, solar panels or a combination of both (hybrid).

The energy coming from the sun depends on the wavelength, leading to the solar spectrum [12]. The standard spectrum for space applications is referred to as AM0. It has an integrated power of 1366.1W/m^2. Two standards are defined for terrestrial use: the AM1.5 Global spectrum, designed for flat plate modules with an integrated power of 1000W/m^2; and the AM1.5 Direct spectrum, defined for solar concentrator work.

The irradiance depends on a lot of variables such as geographic location, time, plane orientation, weather conditions and albedo (or reflection coefficient of the surface) that represents the reflection on the ground surface. A model was developed based on *r.sun* software [13] to calculate the daily radiation profile for the aircraft mission given the following input data [14]:

- Location: Covilhã, Portugal;
- Time: average daily irradiation profiles in different months;
- Plane orientation: horizontal solar panels.

The output data obtained are the various components of irradiation that are then used to create the graph of the daily irradiance shown in Fig. 7 for the average month of June. In the graph, two characteristic parameters can be obtained: maximum daily irradiation (I_{max}) and daily irradiation time (T_{day}).
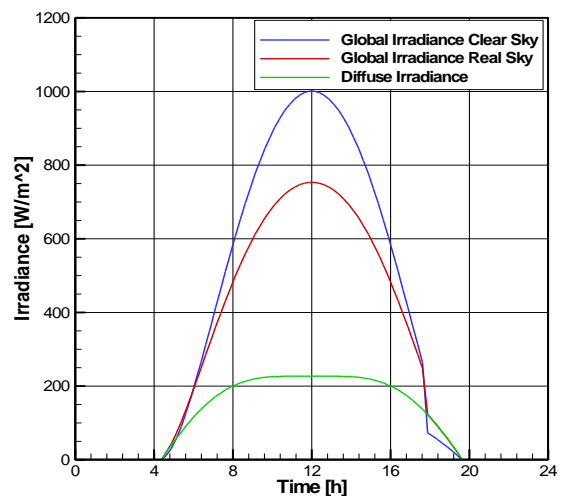

Fig. 7. Daily irradiance (June average).

As mentioned before, the two parameters I_{max} and T_{day} depend on the location and date.

29th Congress of the International Council
of the Aeronautical Sciences
St. Petersburg, Russia; September 7–12, 2014

Figure 8 and 9 show the evolution of these parameters throughout the year for Covilhã, Portugal.
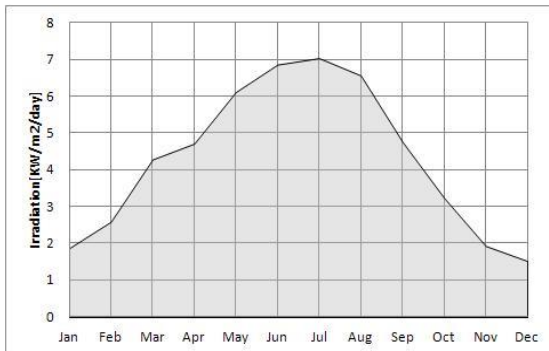

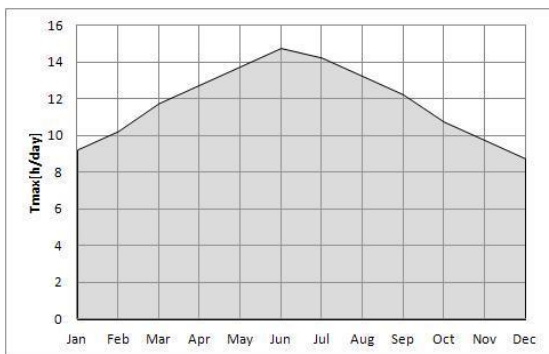Fig. 8. Maximum daily irradiation at the base location.

Fig. 9. Daily irradiation time.

The main components identified in Fig. 5 are discussed next.

A solar panel (also known as module, photovoltaic module or photovoltaic panel) is a packaged, connected assembly of photovoltaic (PV) cells. PV modules are usually made from arrays of crystalline silicon solar cells. These cells are made of extremely thin silicon wafers (about 300μm) and hence are extremely fragile. To protect the cells from damage, an array of cells is hermetically sealed between a layer of toughened glass and layers of ethyl vinyl acetate. There are three types of silicon solar cells according to the type of crystal: monocrystalline, using pure semiconducting material for high level of efficiency but at a high cost; polycrystalline, composed of crystal structures of varying sizes for reduced cost but less efficient; and amorphous, or thin-layer cell, where silicon film is deposited on glass or other substrate material. From all the different efficiencies of the components that influence the use of energy, the most important factor is the solar irradiance and the ability that the solar panels have to harvest that energy, that is, their efficiency. An ideal (perfect) solar cell that would cover the entire spectrum and convert all this energy into electricity would have an efficiency of 100%. In reality, depending on the semiconductors used, only a part of this spectrum is covered. The ratio of converted energy to the received radiation energy define the efficiency of a photovoltaic cell,

$$\eta_{PV} = \frac{P_{PV}}{I_{max} \cdot S_{PV}} , \qquad (8)$$

where P_{PV} is the cells power output (in Watts), I_{max} is the input irradiance and S_{PV} is the surface area of the solar cell. The efficiency is measured under standard test conditions (STC): I=1000 W/m^2, air-mass 1.5 reference spectral distribution (corresponding to the AM1.5 global spectrum standard) and ambient temperature T=25ºC.

The Solar Charge Controller (SCC) limits the rate at which electric current is added to or drawn from electric batteries. It prevents overcharging and may also prevent completely draining ("deep discharging") a battery.

There are numerous types of rechargeable batteries. Several technologies are available but, currently, the lithium-ion (Li-ion) or lithium-ion polymer (Li-Po) (where the electrolyte is a gel and not a liquid) chemistries are the best concerning energy density, with values of 200 Wh/kg [15].

The Electronic Speed Controller (ESC) is an electronic circuit that controls the speed of the electric motor and can also act as a dynamic brake. Typically it uses high power transistors to adjust the motor power by frequency.

Concerning the electric motor, a Direct Current (DC) motor will be used as it is designed to run on DC electric power supplied by battery and solar panels. By far, the most efficient type is the brushless (BL) type, which uses electronic commutation to create a rotating magnetic field vector that pulls an electromagnet or a permanent magnet. Besides high efficiency, the BLDC motors have high reliability, reduced noise and longer lifetime (no brush abrasion). A solar-powered aircraft

7

requires very high efficiency and low mass electric drives for the propulsion system. It has been shown that a machine with a topology combining a high pole number with an ultra low loss laminated material can be more efficient while guaranteeing low mass and size [16].

The propeller is chosen according to the thrust required, the flight speed and motor combination.

The choice of a hybrid system, with both batteries and solar panels, comes naturally. If a battery-only solution was to be adopted, based on the energy data for the mission shown in Tab. 3 and Fig. 6 and the Li-Po energy density, the estimated mass of the battery would be $m_{bat} = E_{req}/E_{bat}^*$=3.01kg, where it was considered a primary battery for propulsion with a capacity of 455.1 Wh (1638.2 kJ) and a secondary battery for avionics with a capacity estimated to be 146.7 Wh, thus totaling 601.8 Wh capacity. Recalling that the estimated total aircraft weight is about 5kg, it is clear that a battery only solution is not possible due to its excessive weight.

Considering the use of solar panels, the selected PV cell is the monocrystalline SunPower C60 [17] because it has the best characteristics in terms of high efficiency, flexibility and low weight. Being the cell dimensions 125x125mm, the maximum number of PV cell can be calculated as

$$N_{SC} = Floor\left(\frac{S_{PV}}{S_{SC}}\right) ,\qquad(9)$$

where S_{SC} is the area of a single PV cell. Therefore, it will be possible to install 44 PV cells, generating a set of 22 arrays per wing as shown in Fig. 10.
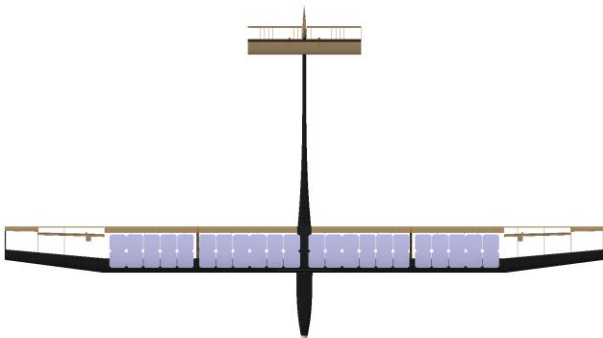

Fig. 10. Solar cell layout (in grey) on LEEUAV wing.

However, as these solar panels comprised of 44 SunPower C60 cells do not provide the required power for the climb segment, the primary battery will be sized for that.

In the months of high solar irradiation, the solar panels offer an excess of energy during the cruise segment, as illustrated for the month of July in Fig. 11.
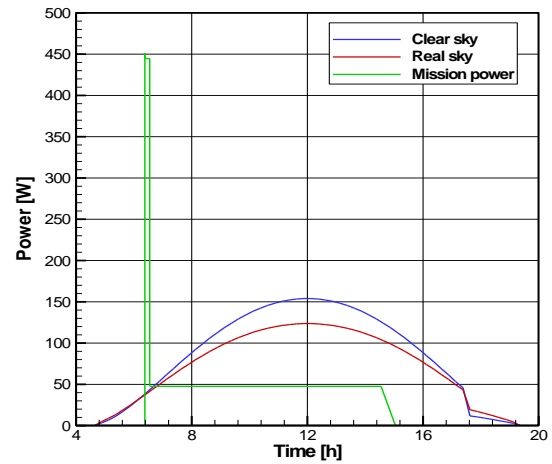

Fig. 11. Power provided by the solar panels in July and mission power required.

Thus, the primary battery must have enough power and energy (E_{req_climb}=74.1Wh) for the climb phase, but it can then be recharged in cruise using the excess energy produced by the solar panels (given by the area between the curves), thus potentially extending the endurance. In months of low solar irradiation, there will be an energy deficit, as shown in Fig. 12 for the month of December.
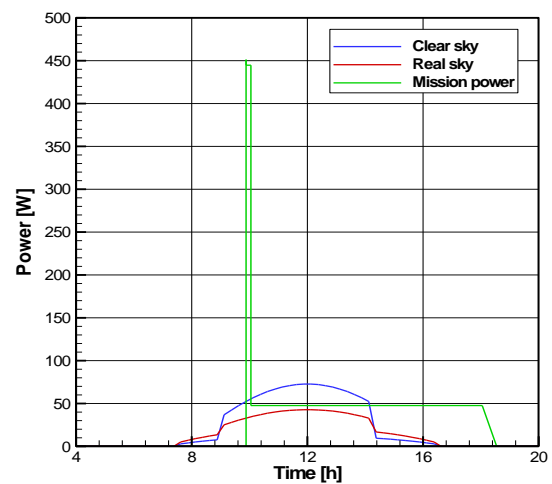

Fig. 12. Power provided by the solar panels in December and mission power requirement.

29th Congress of the International Council
of the Aeronautical Sciences
St. Petersburg, Russia; September 7–12, 2014

In this case, the battery is hardly recharged in flight due to the low power output of the solar panels, and if one wished to satisfy the 8-hour endurance, a much larger battery would have to be installed to provide the estimated deficit of E_{bat}=425.4Wh to complete the mission. If this same analysis is carried out for the equinox months, March and September, the total energy required for the mission with an 8-hour cruise is fully balanced by the energy collected by the solar cell arrays.

In summary, the propulsion system consists of 44 solar cells and a rechargeable battery with a capacity of 74.1 Wh. In these conditions, the solar UAV may only satisfy the mission requirements during the summer months, between March and September.

Following the sizing of the propulsive system, the most appropriate reference of each component was selected according to the calculated requirements.

The solar panel will be made of SunPower C60 cells whose main characteristics are shown in Tab. 4 and Fig. 16 [17].

P_{mpp}	η_{SC}	V_{mpp}	I_{mpp}
3.34 W	22.6%	0.583 V	5.94 A

Tab. 4. Electric characteristics of SunPower C60 solar cell at STC [17].
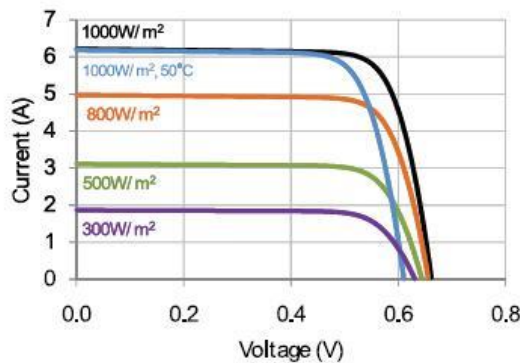

Fig. 13. SunPower C60 current vs voltage curve [17].

Since a single solar cell produces about 0.5 Volts (V_{mpp}) and the propulsion system will work at a nominal voltage of 12V, the cells are connected in a configuration of 22 cells in series per panel on each wing, then connected in parallel between them, to double the current.

Given that the solar panels in parallel are expected to deliver currents up to 12 A

($2 \times I_{mpp}$), the Genasun GV-10 solar charger controller was selected [18]. It is a Maximum Power Point Tracking (MPPT) for lithium batteries controller rated for 10 A continuous current.

The battery selection depends solely on its capacity since the nominal voltage is fixed at 11.1 V corresponding to three Li-Po cells connected in series (3S). To allow a flight with hybrid propulsion with a minimum capacity of 74.1 Wh (6676 mAh) and for additional safety two Hyperion G3 Ex 3S 4200mAh connected in parallel were chosen.

The electric motor and propeller combination are selected to satisfy the maximum power requirement during the mission profile that happens in the climb stage (450W). Hyperion motors were chosen for their efficiency, and reasonable weight and cost.

Motor	Propeller	Voltage	Current	Electric Power	Propulsive Power
Hyperion ZS3020-8	APC 11x5.5E	11.1 V	49 A	545 W	272 W
Hyperion ZS3025-10	APC 15x8E	10 V	51 A	514 W	257 W

Tab. 5. Propeller-motor experimental power data [19].

The data shown in Tab. 5 is not so simple to obtain because the efficiency of the propeller depends on many factors, such as flight speed, throttle setting, rotational speed and advance ratio, and the combination of these values will only be achieved through an experimental test. The propulsive power shown in Tab. 5 was estimated as

$$P_{Propulsive} = \eta_M \cdot \eta_P \cdot P_{Electric}, \qquad (10)$$

with motor and propeller efficiencies of η_M=89% and η_P=50%, respectively, were assumed. The two possible motor and propeller combinations presented provide values close to the desired target.

The appropriate ESC must be able to work with currents higher than the maximum current that the electric motor draws, so the selection of the electric motor and ESC are strictly linked. The Graupner T70 was selected, capable of handling up to 6S LiPo batteries and 70A continuous current.

4.2 Aerodynamic Design

A numerical aerodynamic analysis process that can handle parameterized aircraft geometries was implemented using python, FreeCAD and StarCCM+. The developed computational process enables the swift design of different UAV configurations and their high-fidelity aerodynamic analysis.

FreeCAD [20] was the selected CAD tool for the LEEUAV design. This open-source software proved to be very efficient in the parametric modeling as it allows its functions to be accessible using Python scripts. It can import and export file in formats such as STEP, IGES and STL which can then be used by the CFD software. The design script was divided into five main parts: the loading of the FreeCAD modules, the definition of the UAV geometry parameters, the geometric validation of those parameters, the building and assembly of the components and the export of the object to be later used by the CFD software. The design scripts divide the geometry into four different but dependent geometries, namely its wings, fuselage, tail and nose. A sample is shown in Fig. 14 using the dimensions in Tab. 1. It should be noted that a change in the topology can be quickly adapted in the script.
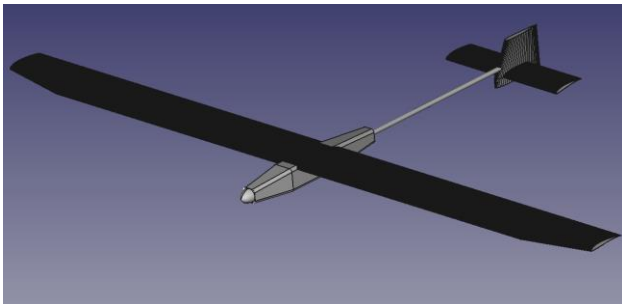

Fig. 14. Model for CFD analysis.

The half wing is defined by four sections at selected spanwise locations, where the airfoil coordinates, chord, wing sweep, twist and dihedral angles are specified. The fuselage is defined using a total of ten different cross-sections placed along its longitudinal axis. The tail, defined similarly to the wing, uses a total of five sections. The spinner and propeller are not modeled, but instead a simple ellipsoid geometry was produced to emulate the nose.

The control volumes employed in the aerodynamic simulations and used to refine specific areas of the aircraft meshes were developed using the design script. A total of five parallelepipedic control volumes were defined: two control volumes that cover the entire wing, another control volume that encompasses the aircraft geometry comprised between the nose and half the tail boom, a fourth control volume that contains the entire aircraft and a fifth that serves as the aerodynamic simulation control volume.

The mesh and aerodynamic model studies in CD-adapco's Star-CCM+ [21] were carried out on simpler geometries because there was no wind-tunnel data for the LEEUAV airfoil. The LEEUAV was designed to fly at Reynolds numbers regimes of about 1.6×10^5 and Mach numbers of approximately 0.02, corresponding to air properties at 1,000 m above sea level, airplane mean chord of 0.35 m and design cruise speed of 7.6 m/s. Two airfoils, MA409 and CAL1215J, at Reynolds numbers similar to that of the LEEUAV during its cruise flight phase were selected from the low-turbulence subsonic wind-tunnel database of the University of Illinois at Urbana-Champaign (UIUC) Aerodynamics Research Laboratory [22]. Two turbulence and transition models were employed in the validation tests: the Spalart-Allmaras (SA) turbulence model [23] that was sporadically employed with the Turbulence Suppression model, and the k-ω SST turbulence model [24] that was always used with the γ-Re$_\theta$ [25] transition model. The comparison between the airfoil simulations and experimental data shown in Fig. 15 proved that both turbulence models at either Reynolds number can accurately determine the lift coefficient but the SA turbulence model fails to provide acceptable results for the drag coefficient. As such the SST model together with the γ-Re$_\theta$ transition model was selected for the remaining analyses.
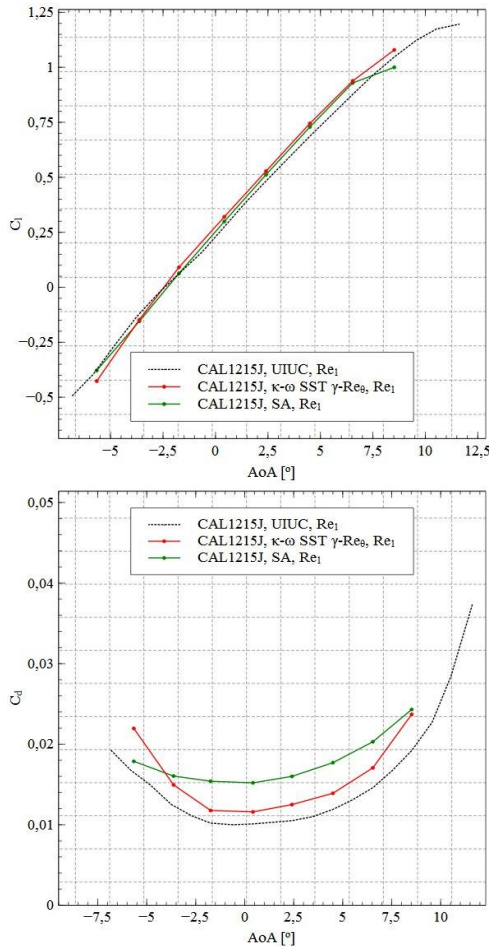
29th Congress of the International Council
of the Aeronautical Sciences
St. Petersburg, Russia; September 7–12, 2014

Fig. 15. Turbulence model validation (Re=2x10^5).

Following the validation tests, a series of aerodynamic simulations using XFOIL and Star-CCM+ were performed on the LEEUAV airfoil at the design Reynolds number. Since the LEEUAV uses solar panels as part of its hybrid propulsion system, their placement on the wing might produce effects similar to those of boundary layer trips. To address this concern, two studies reproducing the effects of having offset surfaces on top of the airfoil were performed. These studies consisted of having two panel configurations: in configuration 1 a panel is placed on top of the original airfoil, thus increasing its thickness and adding two steps to the airfoil upper surface; in configuration 2 a tilted panel is added in order to have the panel trailing edge overlapping with the airfoil surface while maintaining the previous leading edge step. The solar panels used in these studies have a thickness of 2 mm (to account for PV cell encapsulation and attachment to wing surface) and length of 256

mm (corresponding to two PV cells in tandem). Both solar panel configurations promote the generation and fixation of a laminar separation bubble at their leading edge step. The implications are the forced transition at that location with the inherent drag penalties due to turbulence.
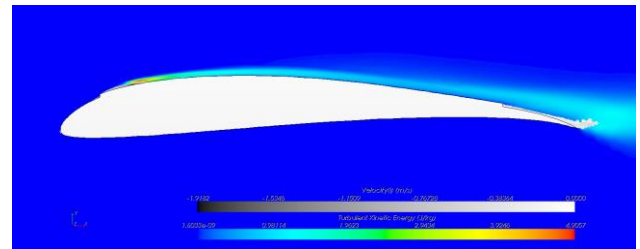

Fig. 16. Solar panel configuration 1, turbulent kinetic energy (J/kg) and regions of reversed flow, AoA=5°.

Figure 16 shows the turbulent kinetic energy generation and regions of reversed flow around solar panel configuration 1 at an angle of attack of 5 degrees. Figures 17 and 18 show the comparison between the lift, quarter-chord point pitching moment and drag coefficients of the clean airfoil and both solar panel configurations. It can be concluded that placing a solar panel on top of the airfoil produces enormous penalties in both the lift and drag coefficients at any angle of attack, consequently, the solar panels ought to be installed inside the wing, or if not, there is the need to implement a smooth surface transition between the airfoil and solar panels.
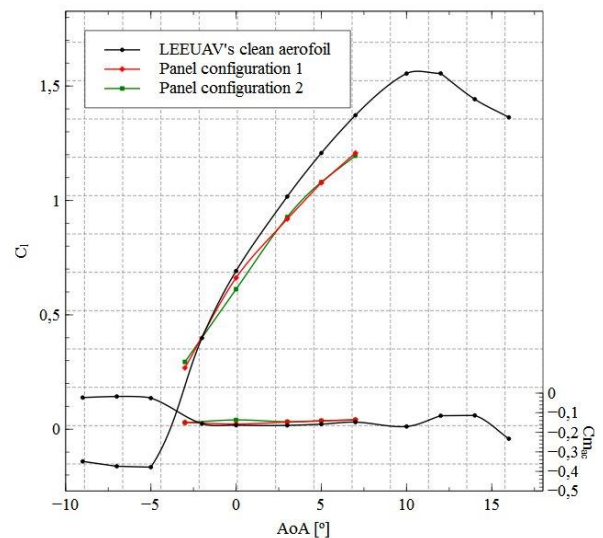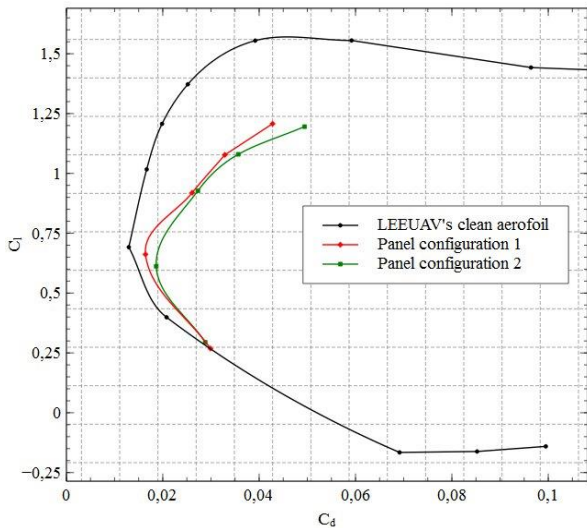

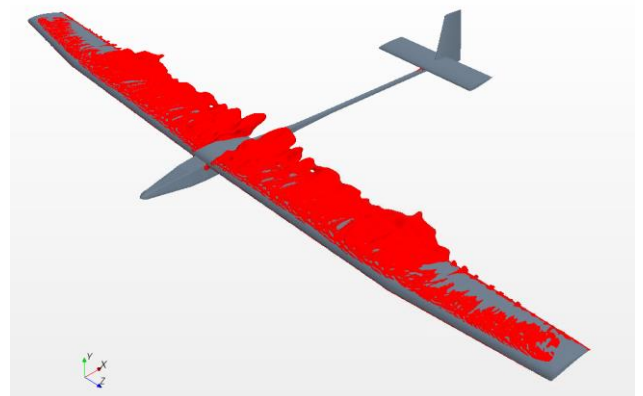Fig. 17. LEEUAV airfoil Cl versus AoA.

Fig. 18. LEEUAV airfoil Cl versus Cd.

The physical models and settings employed in the full three-dimensional LEEUAV analyses are the same as those used in the two-dimensional analyses. Following a grid study, a mesh with approximately 7 million cells was found to be adequate for the three-dimensional aerodynamic simulations. The flow behavior and its intrinsic consequences found on the LEEUAV airfoil are present on the wing: the flow undergoes natural transition on the wing surfaces thus creating laminar separation bubbles. The wing upper surface presents laminar separation bubbles at every simulated angle of attack and every bubble occupies approximately 90% of the wingspan. Figure 19 shows the wing upper surface bubble at 0º. In the angle of attack range of 2º to 4º, the bubble naturally keeps moving closer to the leading edge but its width now increases to values of approximately 45% chord. As the angle of attack increases even further, a region of separated flow starts to develop at the wing root and starting at the wing leading edge. Figure 20 shows this region of separated flow at an angle of attack of 10º, where a loss of aileron control might occur due to the large extent of flow separation at the trailing edge of the wing outer portion.
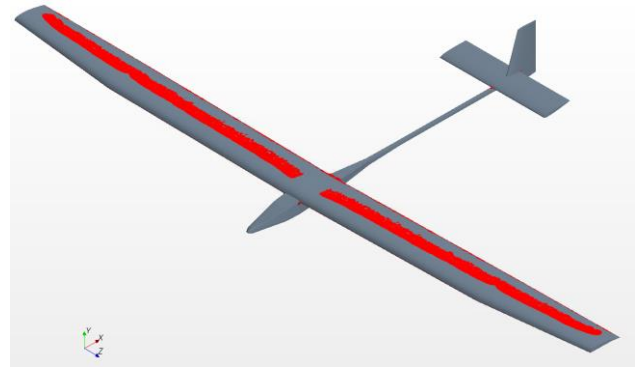
Fig. 19. Spanwise upper laminar separation bubble, AoA=0º.
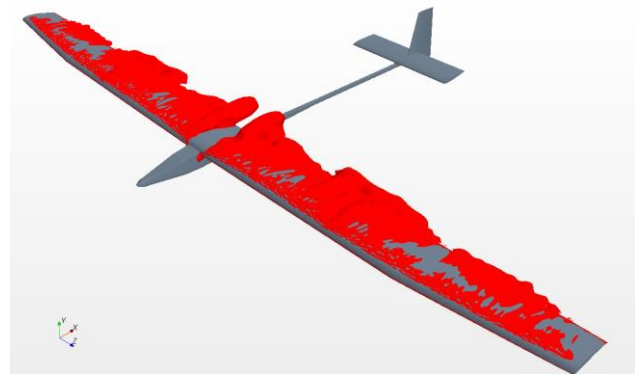
Fig. 20. Wing upper surface flow separation, AoA=10º.

This can be easily fixed if wing washout is used to reduce the lift coefficient at the outer wing section. Figure 21 shows this for a 4-degree tip down twist applied linearly at the trapezoidal part of the wing.

Fig. 21. Reduced flow separation with wing washout, AoA=10º.

29th Congress of the International Council
of the Aeronautical Sciences
St. Petersburg, Russia; September 7–12, 2014

Figures 22 and 23 show the lift, quarter-chord pitching moment and drag coefficients at the simulated angles of attack. A total of eleven angles of attack were simulated from -10º to +10º, with 2º increments. The moment coefficient, obtained at the quarter-chord point, evidences that the LEEUAV, as it was designed, is naturally stable. At positive angles of attack it produces a pitch-down moment whereas at negative angles of attack its tendency is the opposite.
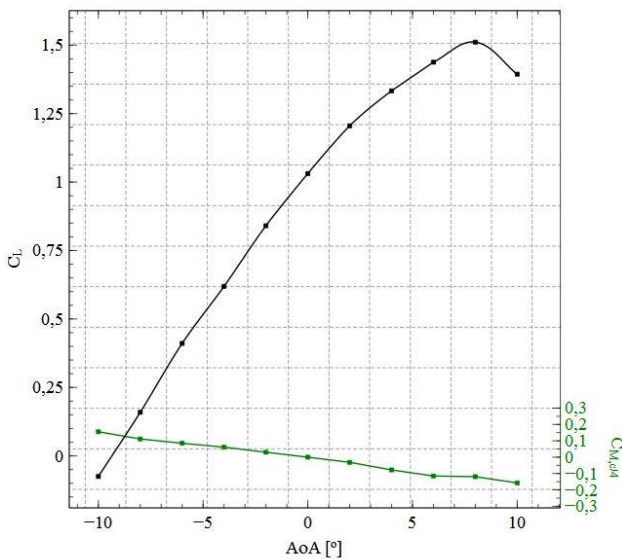

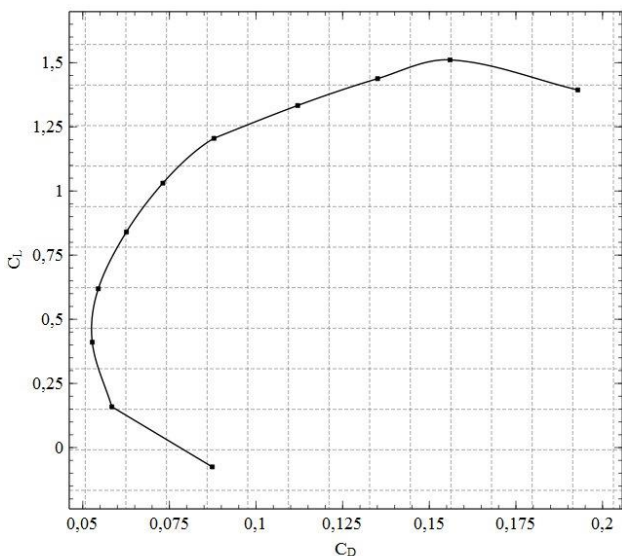Fig. 22. LEEUAV C_L and $C_{M,c/4}$ versus AoA.

Fig. 23. LEEUAV C_L versus C_D.

Table 6 summarizes the LEEUAV aerodynamic performance data. The stall speed was determined to be 6.2 m/s, maximum cruise speed 29.3 m/s and maximum lift-to-drag ratio of 14 for a lift coefficient of around 1.

C_{Lmax}	1.51
$\alpha_{C_L\,max}$	8º
α_{0lift}	-9.5º
$C_{L\alpha}$	5.59 rad^{-1}
C_{Dmin}	0.0527
$C_{D,0}$	0.06
$C_L/C_{D\,max}$	14.01
$\alpha_{C_L/C_D\,max}$	0º
$C_L^{3/2}/C_{D\,max}$	15.06
$\alpha_{C_L^{3/2}/C_D\,max}$	2º

Tab. 6. LEEUAV aerodynamic performance.

4.3 Communication and Electronics

The avionic systems required for the UAV to be either remotely piloted (in RPV mode) and to fly autonomously have been identified. Four important subsystems are being designed and tested: video transmission and on-screen display, long-range radio-frequency control, and autopilot.

In order to perform long range flights without line of sight, a first person view (FPV) system is required. The FPV system is made up by two major assemblies: the ground control station (GCS) and the airborne components. The main function of the FPV GCS is to allow the pilot to see real-time video feed of the UAV, as if he were on a real cockpit. The components of the assembly are a 1.3GHz analog video receiver, an LCD screen, a digital video recorder that records all flight videos to a memory card, two battery voltage checkers, a power module that distributes the power to all the ground station equipment and contains a video buffer that ensures a clean video signal to all connected devices and finally two Li-Po batteries that power all the ground station equipment. The video receiver is connected to either a skew planar wheel or a heliaxial high directivity (11dBi) antenna. The latter is used when long range is desirable and the former for close range flights (less than 3km). The video display screen is a high brightness 12.1" LCD that has the particularity of not having a blue screen when the signal strength is weak. This is of utmost importance because in the case of video signal degradation, the monitor will continue to show the noisy video feed. The battery packs are sized to provide power for

more than 12 hours of continuous operation. The control ground station is shown in Fig. 24 with two different video receiver antennas.

Fig. 24. Complete ground control station showing the video receiver connected to: left) skew planar wheel antenna and right) heliaxial high directivity antenna.

The main airborne components are a video camera with pan and tilt motion, a microphone, an On-Screen Display (OSD) that receives data from the built-in autopilot telemetry and overlaps all the relevant data for piloting purposes on the video signal before being broadcasted, and a transmitter that feeds the video signal to the GCS. All the referred components are assembled in a detachable pod to allow an easy and fast installation and also to allow easy access to the fuselage interior. The airborne components are powered up using the balance charge plug of the flight battery. In order to avoid noise coming from the brushless motor on the video signal, an LC filter is used in series with the flight battery. The pan and tilt support is made of laser cut plywood and is actuated by two micro servos. The video transmitter has 600 mW of radiated power and is equipped with a skew planar wheel which is a low directivity circular polarized antenna. All the FPV antennas use circular polarized antennas since they have two distinct advantages: multipath interference is rejected, and polarization is not lost when the aircraft is banked during a turn. The airborne FPV system components are shown in Fig. 25 mounted on a Skywalker UAV for testing purposes.
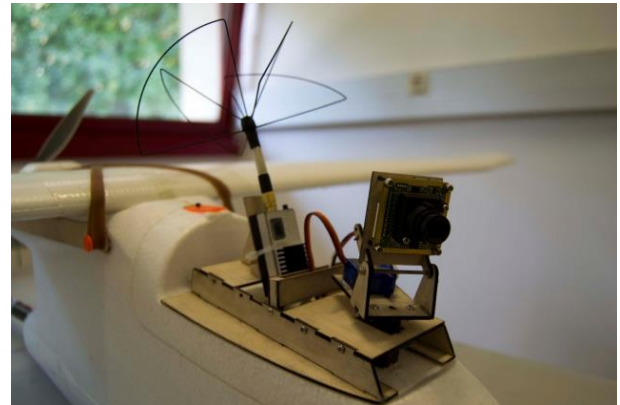

Fig. 25. Sample detachable pod carrying the airborne FPV system components.

In order to fly safely long distances, a reliable radio control link is essential. For that purpose a Thomas Scherrer Long Range System (LRS) [26] attached to a Multiplex royal EVO 9 radio is used. This LRS has been used since 2008 in the most diverse applications both civil and military with very good results. The radio is connected to the transmission module through the PPM (Pulse Position Modulation) external port of the RC system. It operates through the UHF band (433 MHz to 440MHz), has a maximum radiated power of 2W with Frequency Hopping Spread Spectrum (FHSS). The receiver has a total of 12 output channels and has an RSSI (Receiver Signal Strength Indication) output that indicates the signal strength. It also has a PPM output that is very convenient, because it dramatically reduces the wiring between the receiver and the autopilot to just only two cables, one being the RSSI and other the PPM out. In Fig. 26 it is possible to observe the complete system. This is a totally portable system, user friendly, easy to operate with minimum knowledge of the system and it is also assembled in a short time period. Only two people are required for operating this system, one at the control of the UAV and the other monitoring the UAV flight telemetry on the computer.

29th Congress of the International Council
of the Aeronautical Sciences
St. Petersburg, Russia; September 7–12, 2014

Fig. 26. Complete System with the SkyWalker UAV.

Although sophisticated autopilot systems are able to plot their way through winds of varying speeds, keeping gliders aloft indefinitely [27], this first generation LEEUAV makes use of an affordable off-the-shelf system. The autopilot system that is intended to be used on the UAV is the ArduPilot Mega 2.5 (APM 2.5) which is interfaced and controlled using the ArduPlane, an open source autopilot software [28]. This system is capable of transforming any kind of aerial vehicle on a fully autonomous vehicle that can perform programmed missions through waypoints. In the present case, the autopilot is essentially used as a platform for acquiring all kinds of sensor data and sending this data to the telemetry ground station to record it and later post-process it. This system is composed by two main sub-systems: the autopilot board and the telemetry ground station.

The autopilot board has several internal sensors such as 3-axis gyros, 3-axis accelerometers, a magnetometer, a GPS system and a barometric pressure sensor. With this autopilot it is possible to add other external sensors. The external sensors used on the UAV are a differential pressure sensor that is used for determining the airspeed, a voltage and current sensor that are included in the power module that also feeds the autopilot via a linear regulator and a RSSI signal coming from the receiver. This board has 8 standard RC channel inputs (PWM) but only one is used since the RC receiver is feeding the APM with a PPM signal that synthesizes all the 8 channels. The outputs are connected to all the servos and the speed controller of the motor. The APM uses

the 3DR uBlox LEA-6H GPS which will be fitted on the wing, away from electromagnetic noise generated by the electrical motor and the video transmitter. The autopilot board is installed in the fuselage underneath the wing, at the centre of gravity of the UAV.

The telemetry ground station is constituted by a laptop with the Ardupilot Mission Planner software and a 2.4GHz FHSS Laird Module with standard 2dBi dipole. The Ardupilot Mission Planner is an open source autopilot software [28] where the autopilot can be tuned and the missions can be programmed. Furthermore, all the telemetry data can be shown and stored with this application. This software was chosen because it has a good interface and it is very intuitive when configuring the autopilot. When using the Autopilot mode, it is necessary to define waypoints and Ardupilot Mission Planner interfaces with Google Maps to facilitate waypoints positioning. The waypoints are then transferred to the APM 2.5 and the autopilot controller ensures that the UAV will follow the defined waypoints coordinates. There are also other flight modes that can be triggered: Stabilize, Fly By Wire (FBW), Return To Launch (RTL). The RTL mode is very useful because in case of video signal loss or long range radio control system failure, this mode is engaged and the UAV will automatically return to home position.

4.4 Other tasks

Some tests are being performed on the harvesting of solar power with the solar cell arrays placed at different angles to the incoming sunlight and covered with a variety of different thin transparent films. The aim of these tests is twofold. First, a better estimate of the amount and of solar energy collected as the UAV maneuvers during its mission can help predicting more accurately the endurance of the flight and also contribute to plan a more efficient trajectory path along the mission to maximize solar power harvested. Secondly, the type of structure selected for the wings, as described in Sec. 5, requires a film to cover the whole of its surface thus producing its full

aerodynamic shape. With that in mind, it is possible that the solar panels are placed, flush with the airfoil contour, under this film which should be as permeable as possible to the sunlight to minimize power losses. Besides measuring the electrical output power, the solar irradiance is to be measured using a pyranometer to assess the solar panel efficiency under different installation and operating conditions.

Other experimental studies are also underway to characterize a few electrical motors and propellers. A motor and propeller test assembly is being constructed for static and dynamic thrust and efficiency measurement. These tests will provide data to complement the already performed numerical estimates and help selecting the propulsion system with the highest efficiency.

5 Prototype Structure and Construction

A lightweight structure is fundamental for all aircraft, especially for those powered by an electrical battery or solar panels. For that reason, the structural concept developed favors the use of composite materials and wood.

For the wing, a structural layout using a circular carbon fiber reinforced plastic (CFRP) tube for the spar, balsa wood or low density PVC foam for light ribs, plywood for strong ribs and balsa wood for the leading and trailing edge stringers was considered. After some initial sizing and construction trials, that idea evolved to a CFRP D-box containing two small pultruded carbon spar caps and a 0.15 mm CFRP skin laminated around a very low density foam core with plywood for strong aft ribs and balsa wood for light aft ribs and trailing edge stringer. This structural concept for the wing, though slightly heavier than the initial one, provides higher torsional and bending stiffness which is more suitable to accommodate the solar cell arrays on its upper surface. The whole wing is covered with a thin foil of a heat-shrinking material to provide the final aerodynamic shape before the pre-encapsulated solar cells are fixed onto its surface. The initial estimated wing mass of 1.2

kg increased to 1.6 kg owing mainly to the supporting foam inside the D-box.

The wing is divided into three panels that can be disassembled for transportation. The central panel contains two solar arrays each having 12 solar cells and placed symmetrically on either side of the wing central line. The outer panels exhibit a rectangular portion holding the remaining cells and a tapered portion with the ailerons as seen in Fig. 10. Bending moments are transmitted from the outer panel to the central panel by means of two CFRP circular tubes attached via two plywood ribs to the spar: the outer panel has a smaller diameter tube that fits inside another in the central wing panel as shown in Fig. 27. A small CFRP pin near the leading edge transmits torsion moments.
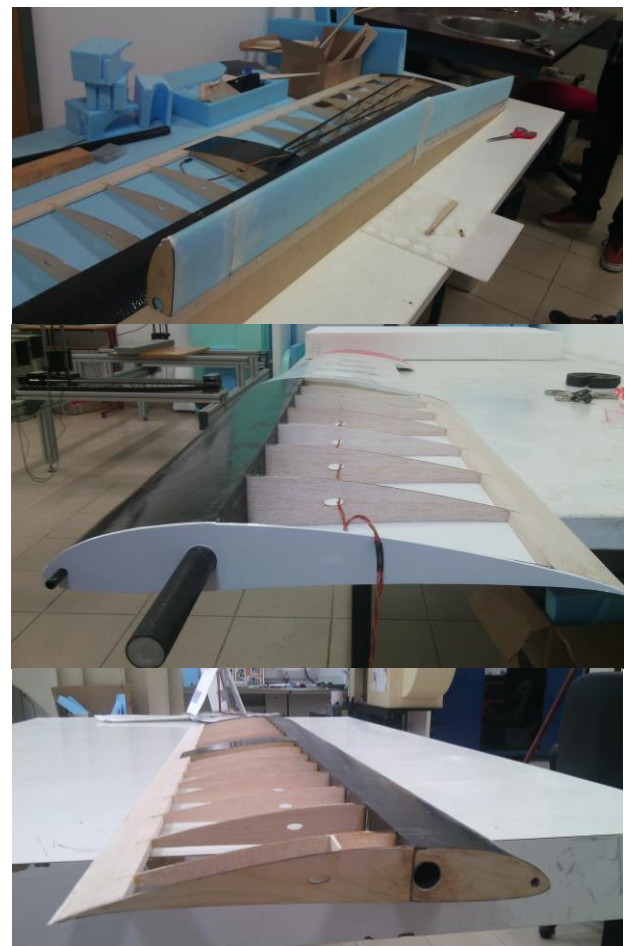

Fig. 27. Some pictures illustrating the wing manufacturing: top) central wing panel on its mounting jig with machined leading edge foam of the left outer panel made of extruded polystyrene; middle) right outer wing panel; bottom) central wing panel.

29th Congress of the International Council
of the Aeronautical Sciences
St. Petersburg, Russia; September 7–12, 2014

Since the tail boom is quite long the tail must be light for balance reasons. Also, the control loads are low due to the long moment arm about the center of gravity. In this case, a structure comprising balsa wood spar webs, leading and trailing edge stringers and ribs with small rectangular cross section pultruded carbon rods for the spars are used for both the horizontal and vertical stabilizers.

The fuselage is of the monocoque structural type with the skin made of CFRP and reinforced with frames where concentrated loads are applied (loads from motor and wing, for example).

6 Flight Testing

Flight testing serves two important purposes. Firstly, qualitative information on the flight characteristics, including performance and handling, can be gathered by the pilot. Secondly, by having the vehicle instrumented with appropriate sensors, processing and communications hardware, the flight parameters can be monitored in real time and recorded for subsequent analysis and performance estimation. Of course, the main objective of the flight testing is to confirm the LEEUAV specifications, in particular its endurance and flight speed, and to validate the models and the methodology used in the design process.

The systems for performing these tasks are already available and were described in Sec. 4.3. What is required now is an airframe flightworthy to proceed with the design validation.

An initial prototype (Fig. 28), with the same geometry and size as the evaluation prototype but using a much simpler structure made primarily of reinforced polystyrene foam and equipped only with a battery pack and a smaller motor, was built to assess the takeoff performance and its general handling qualities in flight. A buggy which stays on the ground after takeoff was developed to allow the UAV, which does not have a landing gear, to move on the ground and to takeoff by its own means. A takeoff run distance of less than 5 m was

demonstrated. Climb performance and handling qualities are adequate for the mission specified.

Fig. 28. Initial prototype standing on the buggy and ready for takeoff.

The new wing is complete and it has been installed on the existing initial fuselage after ground structural loading tests have been performed up to 3G loads. Deflections were within predicted values and no permanent deformations of the structure and of connecting elements were observed. A first flight was carried out to qualitatively evaluate the wing in flight (Fig. 29).
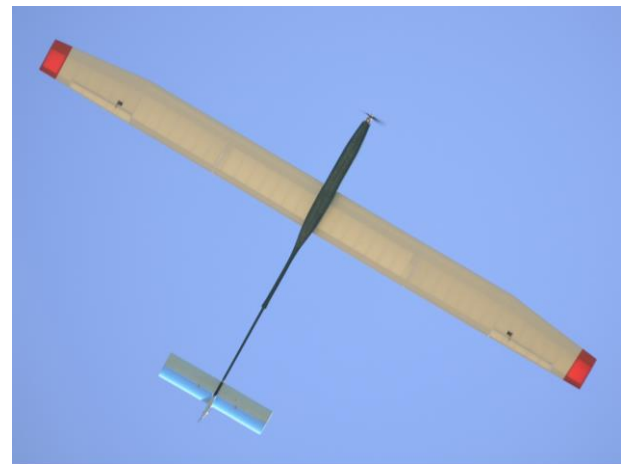

Fig. 29. First flight of the new wing installed on the initial fuselage.

Flight testing of the LEEUAV prototype will resume after the proper fuselage and tails' manufacturing is finished and ground testing is complete. Initial flights with remote control will be performed to assess the general flight characteristics of the vehicle with the new stiffer wing and to calibrate all sensors.

17

Then, the solar panels will be attached onto the wings for endurance tests which will be performed both in RC and autonomous flight modes.

7 Conclusions

An electric UAV capable of harvesting sun light and perform a long endurance mission was designed using in-house low fidelity analyses and optimization tools and commercial high fidelity software packages.

Lightweight materials and efficient structural concepts were used to take advantage of the aerodynamic design and propulsion system to attain the maximum overall energy efficiency possible.

An initial prototype was developed to qualitatively assess the flight handling characteristics of the UAV. The flights carried out indicate that stability and control response are adequate and that climb and glide capability is in line with predictions.

A second, stiffer and more accurate wing was built for structural validation. This component will be part of a second complete prototype meant to be used for further structural validation, systems integration and full mission evaluation.

The LEEUAV design is expected to become a reference in the Portuguese UAV community, in particular in academia. It is supposed to become a working platform for research and future developments.

Acknowledgments

References

[1] Federal Aviation Administration, *Unmanned Aircraft Systems*, USA, www.faa.gov/about/initiatives/uas/, 2014.

[2] AUVSI Association for Unmanned Vehicle Systems International, USA, www.auvsi.org, 2014.

[3] AeroVironment RQ-20 Puma AE, USA www.avinc.com/uas/small_uas/puma/, 2014.

[4] Insitu ScanEagle X200, USA www.insitu.com/systems/scaneagle, 2014.

[5] Solar Impulse 2, Round-The-World Solar Airplane, Switzerland, www.solarimpulse.com, 2014.

[6] LAETA. *Associated Laboratory for Energy, Transports and Aeronautics*. Portugal.

[7] CCTAE. *Center for Aerospace Science and Technology*. Lisbon, Portugal.

[8] AEROG, *Aeronautics and Astronautics Research Center*, Covilhã, Portugal.

[9] IDMEC. *Institute of Mechanical Engineering*, Lisbon, Portugal.

[10] H. Karakas, E. Koyuncu and G. Inalhan, *ITU Tailless UAV Design*, Journal of Intelligent & Robotic Systems, vol. 69, n.1-4, pp 131-146, 2013.

[11] M. Drela, XFOIL: An Analysis and Design System for Low Reynolds Number Airfoils, Lecture Notes in Engineering, vol.54, pp 1-12, Springer, 1989.

[12] NOAA National Oceanic & Atmospheric Administration, USA, www.esrl.noaa.gov/gmd/grad/about/rad.html, 2014.

[13] GRASS Geographic Resources Analysis Support System, grass.osgeo.org, 2014.

[14] JRC-PVGIS Joint Research Centre Photovoltaic Geographical Information System, re.jrc.ec.europa.eu/pvgis, 2013.

[15] G. A. Nazri and G. Pistoia, Lithium Batteries Science and Technology, ISBN:9781402076282, 2003.

[16] B. C. Mecrow, J. W. Bennett, A. G. Jack, D. J. Atkinson and A. J. Freeman, *Drive Topologies for Solar-Powered Aircraft*, IEEE Transactions on Industrial Electronics, vol.57, n.1, 2010.

[17] SunPower C60 Solar Cell Mono Crystalline Silicon, us.sunpower.com, 2014.

[18] Genasun, Solar Charge Controllers http://genasun.com, 2014.

[19] Hyperion, motor test data, http://media.hyperion.hk/dn/zs/ZS30propdata.pdf, 2014.

[20] FreeCAD - *Open Source parametric 3D CAD modeler*, www.freecadweb.org, 2014.

[21] CD adapco STAR-CCM+, www.cd-adapco.com/products/star-ccm, 2014.

[22] G. A. Williamson, B. D. McGranahan, B. A. Broughton, R. W. Deters, J. B. Brandt and M. S. Selig, *Summary of Low-Speed Airfoil Data*, Vol.5, 2012.

[23] P. R. Spalart and S. R. Allmaras, *A One-Equation Turbulence Model for Aerodynamic Flows*, AIAA, 1992.

29th Congress of the International Council
of the Aeronautical Sciences
St. Petersburg, Russia; September 7–12, 2014

*[24]*F. R. Menter, *Two-Equation Eddy-Viscosity Turbulence Models for Engineering Applications*, AIAA Journal, Vol.32, No.8, 1994.

*[25]*F.R. Menter, R. B. Langtry, S. R. Likki, Y. B. Suzen, P. G. Huang and S. Volker, *A Correlation-Based Transition Model Using Local Variables*, Journal of Turbomachinery, Vol.128, 2006.

*[26]*Thomas Scherrer UHF Long Range Systems, Denmark, www.tslrs.com, 2014.

*[27]*Campbell M., *Plane sailing*, New Scientist, Vol. 210, Issue 2818, 2011.

*[28]*APM Autopilot Suite, Arduplane and Mission Planner, www.ardupilot.com, 2014.

Copyright Statement